

Effects of Synthesis and Processing on Optoelectronic Properties of Titanium Carbonitride MXene

Kanit Hantanasirisakul,^{†,‡,§} Mohamed Alhabeab,^{†,‡,§} Alexey Lipatov,[§] Kathleen Maleski,^{†,‡,§} Babak Anasori,^{†,‡,§} Pol Salles,^{†,‡} Chanoknan Ieosakulrat,^{†,||} Pasit Pakawatpanurut,^{||} Alexander Sinitskii,[§] Steven J. May,[‡] and Yury Gogotsi^{*,†,‡,§}

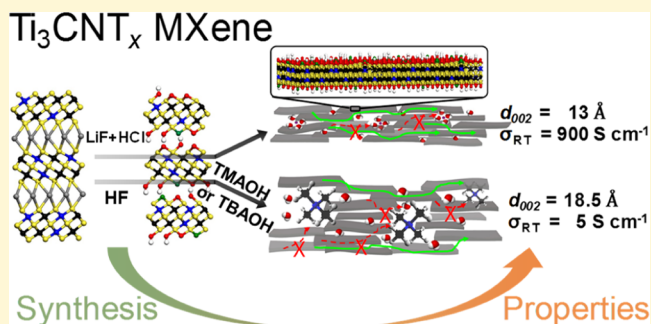
[†]A.J. Drexel Nanomaterials Institute and [‡]Department of Materials Science & Engineering, Drexel University, Philadelphia, Pennsylvania 19104, United States

[§]Department of Chemistry and Nebraska Center for Materials and Nanoscience, University of Nebraska-Lincoln, Lincoln, Nebraska 68588-0304, United States

^{||}Center of Sustainable Energy and Green Materials, Center of Excellence for Innovation in Chemistry, and Department of Chemistry, Faculty of Science, Mahidol University, Bangkok 10400, Thailand

Supporting Information

ABSTRACT: MXenes, a relatively new class of two-dimensional (2D) transition-metal carbides, carbonitrides, and nitrides, exhibit unique properties such as high electronic conductivity, a wide range of optical characteristics, hydrophilicity, and mechanical stability. Because of the high electronic conductivity, MXenes have shown promise in many applications, such as energy storage, electromagnetic interference shielding, antennas, and transparent coatings. 2D titanium carbide ($\text{Ti}_3\text{C}_2\text{T}_x$, where T_x represents surface terminations), the first discovered and most studied MXene, has the highest electronic conductivity exceeding $10\,000\text{ S cm}^{-1}$. There have been several efforts to alter the conductivity of MXenes, such as manipulation of the transition-metal layer and control of surface terminations. However, the impact of the C and N site composition on electronic transport has not been explored. In this study, the effects of synthesis methods on optoelectronic properties of 2D titanium carbonitride, Ti_3CNT_x , were systematically investigated. We show that Ti_3CNT_x , which hosts a mix of carbon and nitrogen atoms in the X layer, has lower electronic conductivity and a blue shift of the main absorption feature within the UV–visible spectrum, compared to $\text{Ti}_3\text{C}_2\text{T}_x$. Moreover, intercalants such as water and tetraalkylammonium hydroxides decrease the electronic conductivity of MXene due to increased interflake resistance, leading to an increase in resistivity with decreasing temperature as observed in ensemble transport measurements. When the intercalants are removed, Ti_3CNT_x exhibits its intrinsic metallic behavior in good agreement with Hall measurements and transport properties measured on single-flake field-effect transistor devices. The dependence of conductivity of Ti_3CNT_x on the presence of intercalants opens wide opportunities for creating MXene-based materials with tunable electronic properties.



INTRODUCTION

Two-dimensional (2D) transition-metal carbides, carbonitrides, and nitrides, collectively known as MXenes, have shown great promise in various applications, including energy storage, electromagnetic interference shielding, transparent conductive coatings, photothermal therapy, catalysis, water desalination, and as a metamaterial.^{1–7} MXenes have a general formula of $\text{M}_{n+1}\text{X}_n\text{T}_x$, where M is an early transition metal, X is C and/or N, and T_x represents surface terminations, such as O and F, and $n = 1–3$. To date, nearly 30 MXene compositions with different properties have been experimentally synthesized and dozens more have been predicted to be stable and studied theoretically. Among them, 2D titanium carbide, $\text{Ti}_3\text{C}_2\text{T}_x$, is the first and most studied MXene. It has high metallic conductivity exceeding $10\,000\text{ S cm}^{-1}$ in thin films.⁸ The

performance of MXenes in the above-described applications is related to their electronic conductivity, which can be improved by different approaches, such as increasing the lateral flake size, minimizing the defects and impurities, and modification of surface terminations.^{9–11} Density functional theory (DFT) studies have predicted that the electronic and optical properties of MXenes strongly depend on transition metals, X elements, and surface terminations.^{12,13} For example, it has been experimentally shown that the composition of outer atomic layers (M') in the ordered double-transition-metal MXenes, $\text{M}'_2\text{M}''\text{C}_2$ and $\text{M}'_2\text{M}''_2\text{C}_3$, has a strong influence on

Received: January 27, 2019

Revised: March 23, 2019

Published: March 25, 2019

their electronic properties.¹⁴ Moreover, the effects of surface terminations and intercalation on the electronic properties of MXenes have been recently reported.^{11,15,16} However, there is no experimental evidence that tuning of the electronic and optical properties of MXenes can be achieved by manipulating the X elements.

In most bulk transition-metal carbides and carbonitrides, the electronic conductivity increases with nitrogen content because of increased density of states (DOS) at the Fermi level (E_F) resulting from the extra electrons of the nitrogen atoms.^{17–20} In bulk-layered ternary carbides and/or nitrides (known as MAX phases, where A is a group IIIA–VIA element), which are precursors for MXene synthesis, the electronic conductivity is of metallic character with high DOS at the E_F .^{21,22} It has been shown that the electronic properties of the MAX phases can be controlled by manipulating the three components of the structure, that is, transition metals, A elements, and X elements.^{23–25} Although alteration of the transition metal and/or X layer affects the DOS at E_F of the MAX phases, the change in the A elements (e.g., formation of a binary solid solution) shows little effect on electronic and thermal properties aside from increased residual resistivity, resulting from solid solution scattering.²⁴ The effects of N-substitution on the electronic properties of the MAX phases are apparent when comparing Ti_2AlC , $Ti_2AlC_{0.5}N_{0.5}$, and Ti_2AlN . $Ti_2AlC_{0.5}N_{0.5}$ showed the highest resistivity followed by Ti_2AlC and Ti_2AlN , and the DOS at E_F slightly increases with N-substitution. Similar trends were observed for Ti_3AlC_2 and Ti_3AlCN systems.²⁵ However, for carbonitride MXenes, it was predicted that the DOS at E_F of Ti_3CNT_x and $Ti_3N_2T_x$ MXenes is lower than that of their $Ti_3C_2T_x$ counterparts, yet these materials are metallic with high DOS at E_F . The Fermi level is positioned at a band that contains mainly Ti 3d states, whereas the C 2p and N 2p states are found between -4 to -2 eV and -6 to -3 eV below the Fermi level, respectively.¹³ Unlike the MAX phases, the contribution of the N 2p band in carbonitride and nitride MXenes to the DOS at E_F is almost negligible. However, this difference in electronic properties between bulk carbonitrides and 2D carbonitride MXenes has not been investigated experimentally. Therefore, it might be possible to alter the electronic conductivity of $Ti_3C_2T_x$ by partial substitution of carbon atoms with nitrogen atoms in the X layer—forming Ti_3CNT_x . Titanium carbonitride MXene has been reported to have very attractive energy storage and electrocatalytic properties,^{26–28} so understanding and controlling its conductivity is of great practical interest. Moreover, we have recently shown that the electronic properties of Mo_2CT_x and V_2CT_x MXenes can be tuned by formation of Mo_2N and V_2N via high-temperature ammoniation.²⁹

Similar to its $Ti_3C_2T_x$ carbide counterpart, Ti_3CNT_x can be synthesized by etching Ti_3AlCN in (i) hydrofluoric acid (HF) followed by intercalation of organic intercalants, such as hydrazine or tetrabutylammonium hydroxide (TBAOH), to delaminate the 2D MXene layers^{30–32} or (ii) in a mixture of lithium fluoride (LiF) and hydrochloric acid (HCl), forming HF in situ, without subsequent use of any organic intercalant.²⁶ For both synthesis methods, Ti_3CNT_x showed much lower conductivity compared to $Ti_3C_2T_x$ obtained by similar methods, although the LiF + HCl method produced MXenes with higher electronic conductivity compared to HF etching.^{9,26,30} However, there is no published report on the effects of synthesis and processing methods on the optoelectronic properties of Ti_3CNT_x MXene.

In this work, we studied the optoelectronic properties of a titanium carbonitride MXene, Ti_3CNT_x , and the effects of material synthesis and processing on those properties. We showed that the presence of nitrogen atoms in the X layer results in lower electronic conductivity and a blue shift of the main absorption peak in UV–visible spectra compared to $Ti_3C_2T_x$. Moreover, we found that the macroscopic electronic transport behavior of Ti_3CNT_x is largely governed by interflake electron hopping processes rather than intrinsic electron transport within a flake. Single-flake measurements reveal intrinsic metallic behavior of the material. This work demonstrates the effects of X elements, synthesis, and processing on optoelectronic properties of MXenes, providing more opportunities to tune those properties.

■ EXPERIMENTAL SECTION

Ti_3AlCN MAX powder was prepared following a procedure reported elsewhere.³² Briefly, elemental Ti (Alfa Aesar, 99.5 wt % purity), AlN (Sigma-Aldrich, 99 wt % purity), and graphite (Alfa Aesar, 99 wt % purity; particle size $< 48 \mu m$) with a molar ratio of 3:1:1 were ball-milled for 18 h in a plastic jar with 10 mm-diameter zirconia milling balls at 50 rpm. The powder mixture was heated under Ar flow (100 mL min^{-1}) in a tube furnace at $10 \text{ }^\circ\text{C min}^{-1}$ to $1500 \text{ }^\circ\text{C}$ and held for 2 h. After cooling down to room temperature, the resulting block of Ti_3AlCN MAX was crushed via drill-milling and sieved through a 400-mesh sieve (particle size $< 38 \mu m$).

Ti_3CNT_x MXene was produced by two etching routes, via a mixture of LiF and HCl and via HF. For the LiF + HCl route, 0.5 g of Ti_3AlCN powder was slowly added to a mixture of 0.8 g of LiF (Alfa Aesar) and 10 mL of 9 M HCl (Fisher Chemical), and the solution was stirred at 500 rpm at $35 \text{ }^\circ\text{C}$ for 24 h. Then, the mixture was washed by adding 150 mL of deionized (DI) water and centrifuged at 3500 rpm (2300 rcf) for 5 min followed by decantation of the clear supernatant. The washing process was repeated four to five times until the pH of the supernatant became close to neutral and the supernatant became dark, as a result of partial delamination of Ti_3CNT_x flakes (d- Ti_3CNT_x). The dark supernatant was decanted and ~ 10 mL of DI water was added to the sediment. The mixture was bath-sonicated (2510, Branson) at 40 kHz for 30 min or manually shaken for 15 min and centrifuged at 3500 rpm for 1 h. The supernatant, consisting mainly of single-layer or few-layer flakes of Ti_3CNT_x , was collected for further processing. For the HF route, 2 g of MAX powder was slowly added to 20 mL of 30 wt % HF aqueous solution (Acros Organics). The mixture was stirred at 500 rpm at room temperature ($20 \text{ }^\circ\text{C}$) for 18 h and washed in the same way as the LiF + HCl method. When the pH of the supernatant became close to neutral, the multilayered Ti_3CNT_x (ML- Ti_3CNT_x) was collected by a vacuum-assisted filtration. An additional 200 mL of DI water was used to rinse the powder. To delaminate the HF-etched Ti_3CNT_x , 1 g of the powder was added to a mixture of 5 mL of tetramethylammonium hydroxide (TMAOH) (25 wt % in water, Sigma-Aldrich) or TBAOH (48 wt % in water, Sigma-Aldrich) and 5 mL of DI water. The mixture was stirred for 12 h at room temperature and then washed with repeated centrifugation (50 mL of DI water for two to three centrifugation times or until the pH of the solution was close to neutral). Finally, ~ 10 mL of DI water was added to the sediment, the mixture was bath-sonicated for 30 min, and centrifuged at 3500 rpm for 1 h to separate single- and few-layer flakes from nonexfoliated multilayered MXenes.

The Ti_3CNT_x thin films were prepared by a spin-casting technique using a spin coater (Laurell Technologies, Model WS-650 Hz, USA). The delaminated MXene solution with a concentration of 5 or 20 mg mL^{-1} was applied to an oxygen plasma-treated microscope slide and spun at various spin speeds from 1000 to 10 000 rpm for 30 s. The films were subsequently dried at 5000 rpm for 15 s. The free-standing MXene films were prepared by vacuum-assisted filtration of the delaminated solution on a porous membrane (3501 Coated PP, Celgard, USA).

Sheet resistance was measured using a four-point probe (ResTest v1, Jandel Engineering Ltd., Bedfordshire, UK) with 1 mm distance between the probes. The measurement was repeated five times at the four corners and the middle of each film. The average values were reported.

UV–visible spectroscopy measurements were conducted using a spectrometer (Evolution 201, Thermo Scientific), scanning from 200 to 1000 nm and normalized at 264 nm. A microscope glass slide and DI water were used as blanks for thin-film and solution measurements, respectively. The extinction coefficients (ϵ) were calculated by the Beer–Lambert law [$A = \epsilon Cl$, where A is the measured absorbance, C is the concentration (g L^{-1}) of MXene in solution determined through gravimetric analysis, and l is the optical path length (1 cm)]. The as-produced solutions were serial-diluted, and extinction coefficients were calculated from the extinction value at the peak maxima in the visible region (λ_{max}).

Dynamic light scattering (DLS) of the d- Ti_3CNT_x solutions was performed using a Zetasizer Nano ZS (Malvern Panalytical) in a polystyrene cuvette. The average particle size was taken over a total of five measurements from each sample.

Scanning electron microscopy (SEM) images were taken with an electron microscope (Zeiss Supra 50VP).

The Ti_3CNT_x MXene flakes were also visualized using a FEI Tecnai Osiris scanning transmission electron microscope equipped with a HAADF detector and a X-FEG high brightness Schottky field emission gun. The accelerating voltage was 200 kV. X-ray diffraction (XRD) patterns were recorded by a powder diffractometer (Rigaku Smart Lab, USA) with Ni-filtered $\text{Cu K}\alpha$ radiation operated at 40 kV and 15 mA. A step size of 0.03° and 0.5 s dwelling times were used to collect the patterns.

Atomic force microscopy (AFM) images were recorded by a Bruker AFM Multimode 8 using a driving frequency of 249 kHz, driving amplitude of 73.85 mV, and scanning frequency between 0.6 and 0.9 Hz.

Transport property measurements were conducted in a physical property measurement system (PPMS) (Quantum Design EverCool II). Free-standing MXene films with a size of 5×5 mm were wired to the PPMS sample puck using a silver wire and a conductive silver paint (Ted Pella, CA). Temperature-dependent resistivity was recorded from 10 to 300 K in a low-pressure helium environment (~ 10 Torr) using the four-point configuration. The film thicknesses were measured by an electronic micrometer (MDH-25M, Mitutoyo, IL). The geometry of the samples and probe spacing were taken into account in resistivity calculation following the standard method.³³ Hall measurements were performed at various temperatures using van der Pauw configuration. The magnetic field was swept between -30 and 30 kOe, and the Hall voltage was measured two to five times at the same magnetic field value. The effect of magnetoresistance was removed by subtracting the Hall resistance in the positive magnetic field regime with their respective negative field values and dividing the difference by 2.

X-ray photoelectron spectroscopy (XPS) spectra were collected in a spectrometer (Physical Electronics, VersaProbe 5000, Chanhassen, MN) using a $100 \mu\text{m}$ monochromatic $\text{Al K}\alpha$ X-ray beam. Photoelectrons were collected at a takeoff angle of 45° between the sample surface and the hemispherical electron energy analyzer. Charge neutralization was applied using a dual-beam charge neutralizer, irradiating low-energy electrons and ion beams. Survey scans were obtained from 1000 to -4 eV binding energy using a pass energy of 117.4 eV, whereas the high-resolution scans were obtained within the interested regions using a pass energy of 23.5 eV. Quantification and deconvolution of the core-level spectra were performed using a software package (CasaXPS Version 2.3.16 RP 1.6). Background contributions to the measured intensities were subtracted using a Shirley function.

Thermogravimetric and mass spectroscopy analyses were performed using a Discovery SDT 650 thermal balance connected to a Discovery mass spectrometer (TA Instruments, DE). The free-standing MXene films with masses around 5–10 mg were dried in a vacuum desiccator at room temperature for at least 24 h prior to the

measurement. Then, they were packed in a $90 \mu\text{L}$ alumina pan and heated to 1500°C at a constant heating rate of $10^\circ\text{C min}^{-1}$ in He atmosphere (100 mL min^{-1}). The furnace was purged with a 100 mL min^{-1} flow of He gas for 1 h before the analysis to remove air residue.

For single-flake device fabrication, the Ti_3CNT_x MXene solution was drop-cast onto a Si/SiO_2 substrate and dried in air, leaving multiple MXene flakes on the substrate. Individual monolayer flakes were identified by optical microscopy and then used for device fabrication. Similar to other 2D materials deposited on the Si/SiO_2 substrate, MXene flakes show color contrast in the optical microscope. Multilayered and folded flakes exhibit higher contrast compared with monolayer flakes, which we used to differentiate between the number of layers. For device fabrication, we selected uniformly colored flakes with the lowest contrast, which were confirmed to be Ti_3CNT_x monolayers by AFM imaging. A Zeiss Supra 40 field-emission scanning electron microscope and a Raith pattern generator were used for electron beam lithography to pattern electrodes on Ti_3CNT_x MXene flakes. Deposition of 3 nm of Cr at a rate of 0.2 \AA s^{-1} and 20 nm of Au at a rate of 0.3 \AA s^{-1} was performed using an AJA electron beam evaporation system at a base pressure of $\sim 7 \times 10^{-9}$ Torr. The electrical characterization of MXene devices was performed in a Lake Shore TTPX cryogenic probe station at a base pressure of 2×10^{-6} Torr using an Agilent 4155C semiconductor parameter analyzer.

RESULTS AND DISCUSSION

Synthesis and Delamination. The XRD pattern of the Ti_3AlCN MAX powder used in this study is shown in Figure S1a. The peak positions and intensity are in good agreement with the previous report.³² We note that there is a small amount of M_4AX_3 and M_2AX phases in the powder as indicated by their (002) peaks at 7.5° and 13.0° , respectively. Moreover, we cold-pressed this Ti_3AlCN powder as well as Ti_3AlC_2 powder with pressure ranging from 250 to 900 MPa and compared the electronic conductivity and density of the resulting MAX powder pellets as shown in Figure S1b. Although the conductivity of Ti_3AlC_2 and Ti_3AlCN pellets increased with increasing the applied pressure because of more efficient interparticle contacts at the grain boundaries, the difference between Ti_3AlC_2 and Ti_3AlCN lies within the error of the measurement. This result and that reported earlier show minimal effect of nitrogen substitution on the electronic conductivity of the Ti_3AlC_2 and Ti_3AlCN MAX phases.^{25,34}

A schematic representation of the two synthesis routes and the structures of the resulting products is shown in Figure 1. In the $\text{LiF} + \text{HCl}$ route, the resulting MXene sheets are

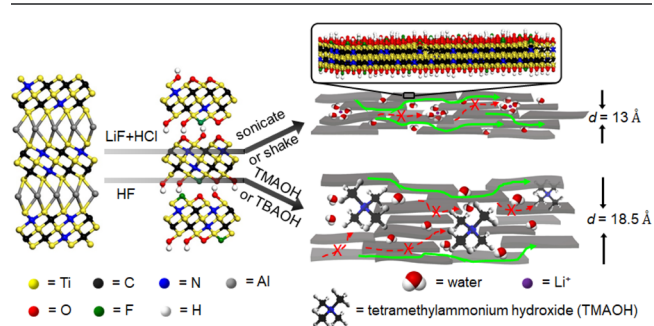


Figure 1. Schematic of the two synthesis routes used for producing Ti_3CNT_x . Using a mixture of LiF and HCl results in Li^+ and H_2O intercalation (upper route), which leads to more compactly stacked MXene sheets compared to when TMAOH or TBAOH are used as intercalants (lower route). Ti, C, N, Al, O, H, F, and Li atoms are represented by yellow, black, blue, gray, red, white, green, and purple spheres, respectively. Electron paths are represented by red and green arrows.

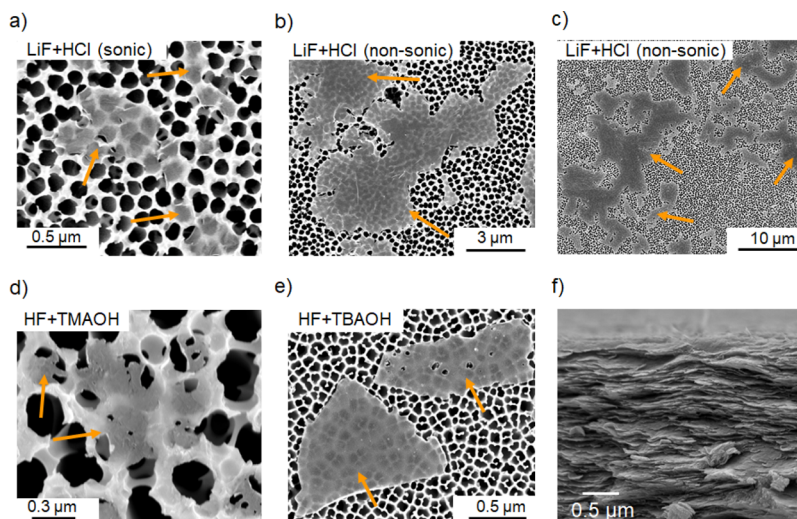


Figure 2. (a–c) SEM images of d- Ti_3CNT_x flakes from the LiF + HCl route with and without sonication. (d,e) SEM images of delaminated Ti_3CNT_x flakes from the HF + TMAOH and HF + TBAOH routes with sonication, respectively. The flakes are marked with orange arrows to be distinguishable from the porous alumina membrane used for imaging. (f) Cross-sectional SEM image of a $\sim 2.5\text{-}\mu\text{m}$ -thick free-standing film prepared by vacuum filtration of d- Ti_3CNT_x (LiF + HCl) solution.

intercalated by water molecules and solvated Li^+ ions, whereas in the HF + TMAOH route, the films are intercalated by water molecules and tetramethylammonium cations (TMA^+). Similar to $\text{Ti}_3\text{C}_2\text{T}_x$, Ti_3CNT_x was readily delaminated without the need of sonication when a mixture of LiF and HCl with a molar ratio of LiF to MAX powder exceeding 7.5:1 was used in the etching step.³⁵ SEM and AFM were used to confirm successful delamination of Ti_3CNT_x via the LiF + HCl route (Figures 2a–c and S2), the HF + TMAOH route (Figure 2d), and the HF + TBAOH route (Figure 2e). Thin and transparent flakes (marked with orange arrows) with lateral size around 300 nm for sonicated solution and up to 10 μm for the LiF + HCl route without sonication were observed over a large area on a porous anodized alumina membrane (Figure 2b–c). A cross-sectional SEM image of a $\sim 2.5\text{-}\mu\text{m}$ -thick free-standing film prepared by vacuum filtration of d- Ti_3CNT_x (LiF + HCl) solution is shown in Figure 2f. Transmission electron microscopy (TEM) and selected area electron diffraction (SAED) of Ti_3CNT_x (LiF + HCl) without sonication also confirm delamination, yielding flakes with lateral size larger than 10 μm with a typical hexagonal symmetry of MXenes (Figure 3). The size distribution curves obtained from DLS of d- Ti_3CNT_x solutions (Figure 4a) are shown in Figure 4b. The DLS results are in good agreement with the flake size observed in SEM and TEM, where the peaks in DLS results are at ~ 300 nm for the sonicated solution and at ~ 1 and 10 μm for

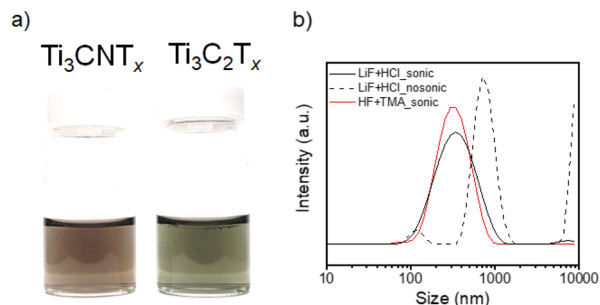


Figure 4. (a) Optical image of d- Ti_3CNT_x and d- $\text{Ti}_3\text{C}_2\text{T}_x$ solution produced by LiF + HCl method. (b) DLS data of d- Ti_3CNT_x solution obtained from different routes. The nonsonicated LiF + HCl route has a larger particle size of 1 μm and a peak of more than 10 μm , which is the upper limit of the DLS machine.

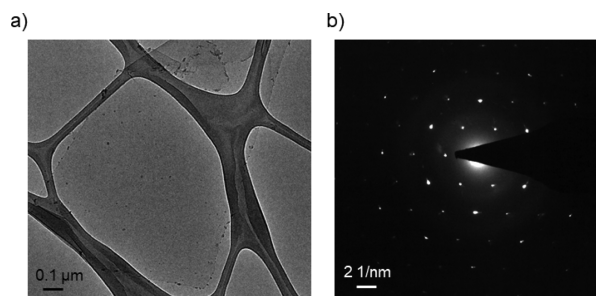


Figure 3. (a) TEM image of a Ti_3CNT_x (LiF + HCl) single flake. (b) SAED pattern showing typical hexagonal symmetry of the flake.

nonsonicated solution. For both synthesis methods, the obtained flakes are free of impurity particles, such as oxide or remaining salt, as can be seen from the clean surface and edges of the flakes in the SEM, TEM, and AFM results in Figures 2, 3, and S2. Nonetheless, small amounts of impurity nanoparticles were observed in the delaminated solution, especially when organic bases were used in the delamination step (not shown). The thickness of a single MXene flake was measured by AFM and was found to be close to 2.5 nm (Figure S2). The thickness of Ti_3CNT_x measured in this work was similar to that of Ti_3CNT_x and $\text{Ti}_3\text{C}_2\text{T}_x$ reported earlier.^{9,26,36} We also observed a step of 1.5 nm when there was a stack of flakes on top of each other. However, the measured thickness values are still larger than that proposed by the DFT calculation and high-resolution TEM images (~ 1 nm).³⁷ The increased thickness is likely due to water and/or other adsorbed molecules trapped between the flakes and the substrate, which was also reported for graphene and other 2D materials.^{38,39}

XRD patterns of free-standing films obtained by vacuum-assisted filtration of the delaminated solution produced by each synthesis method before and after annealing are presented in Figure 5a. For the as-produced films, the (002) peaks of the

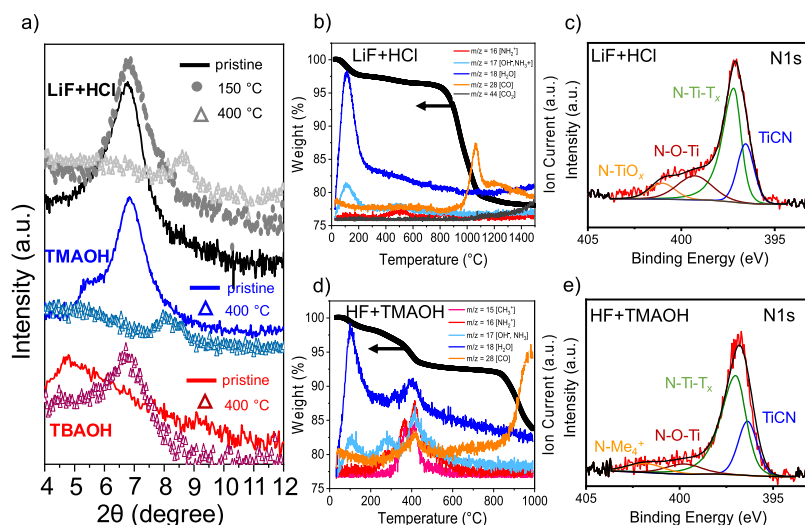


Figure 5. (a) XRD patterns showing the (002) reflection of the Ti_3CNT_x films produced by different methods and post-synthesis treatments. (b and d) TGA–MS thermogram of the Ti_3CNT_x (LiF + HCl) and Ti_3CNT_x (HF + TMAOH), respectively. (c and e) N 1s high-resolution XPS spectra of the Ti_3CNT_x (LiF + HCl) and Ti_3CNT_x (HF + TMAOH), respectively.

LiF + HCl, HF + TMAOH, and HF + TBAOH films are located at 6.8° , 6.8° , and 4.7° , respectively, corresponding to the interlayer distances (d) of 13.0, 13.0, and 18.7 Å, respectively. We used TBAOH to further intensify the effects of intercalated ions on transport properties as will be discussed in the following sections. For the TMAOH-delaminated film, there is a shoulder centered at 5.5° , corresponding to the interlayer distance of 16.1 Å. From the (002) peaks of the as-produced LiF + HCl and HF + TMAOH samples, their interlayer distance is ~ 13 Å because of Li^+ and water intercalation, in good agreement with the previous reports.^{30,40} On the other hand, TMA^+ and TBA^+ intercalation resulted in larger interlayer distances of 16.1 and 18.7 Å, respectively, which are similar to that reported previously.³¹ The increases of ~ 3 and ~ 6 Å for the samples intercalated by TMA^+ and TBA^+ , respectively, agree well with the size of the cations.⁴¹

After drying at 150°C under vacuum for 18 h, a negligible shift was observed in the (002) peak of the Ti_3CNT_x (LiF + HCl) sample. However, when the sample was heated at 400°C in Ar atmosphere for 3 h, the peak shifted to 8.64° (Figure 5a, top pattern). This result suggests that Ti_3CNT_x synthesized by this method has a stronger affinity to the intercalated water molecules compared to $\text{Ti}_3\text{C}_2\text{T}_x$, where the (002) peak was reported to be around 8.6° after drying only at 120°C under vacuum.³⁵ This conclusion is supported by the thermogravimetric analysis coupled with mass spectroscopy (TGA–MS) data shown in Figure 5b, where water desorption (indicated by the $m/z = 18$) was not complete until close to 250°C . The reason for this phenomenon is not clear at the moment and was not observed in the HF-etched samples. After annealing at 400°C , the (002) peaks of the LiF + HCl, HF + TMAOH, and HF + TBAOH samples were at 8.6° (10.3 Å), 8.0° (11.0 Å), and 6.8° (13.0 Å), respectively. The large interlayer spacing of the HF + TMAOH and HF + TBAOH samples after annealing suggests incomplete removal of the organic cations. However, for the HF + TMAOH sample after drying at 400°C , a small peak at 8.6° was also observed, suggesting that some of the TMA^+ cations were removed by thermal annealing. TGA–MS results of the HF + TMAOH and the HF + TBAOH samples shown in Figures 5d and S3a, respectively, show that the organic cations decomposed slightly

after 400°C , which agree with the smaller (002) peak shifts for these two samples compared to the LiF + HCl one. We also tested thermal stability of the TBAOH aqueous solution and found that the sample decomposed at $\sim 250^\circ\text{C}$ as revealed by the thermogram shown in Figure S3b. The increase of the intercalation temperature of approximately 150°C of the intercalated organic species indicates a strong interaction between TMA^+ and TBA^+ ions and the MXene surface, which might be responsible for incomplete thermal decomposition. Independent of the synthesis method, Ti_3CNT_x MXene starts to decompose close to 900°C forming CO gas ($m/z = 28$). Interestingly, no NO_x gas ($m/z = 30, 46$, etc.) was detected after MXene decomposition. The XRD patterns of the sample annealed at 1500°C in He environment (Figure S4a) shows only peaks corresponding to TiN and some trace of anatase and rutile, in contrast to TiC formed when $\text{Ti}_3\text{C}_2\text{T}_x$ is annealed at 1500°C . This result suggests that formation of TiN is thermodynamically more favorable compared to TiC at high temperatures.

XPS was used to analyze chemical composition and C/N ratio of the Ti_3CNT_x prepared by different methods. Shown in Figure 5c,e are high-resolution XPS scans of N 1s region of Ti_3CNT_x prepared from the LiF + HCl and the HF + TMAOH routes, respectively. For the LiF + HCl sample, four peaks were used to fit the spectra: TiCN (396.6 eV), N–Ti–T_x (397.2 eV), –NR₂ (R = C, H) or N–O (399.3 eV), and N–TiO_x (401.0 eV). Similar peak assignments were used for the HF + TMAOH and HF + TBAOH samples (Figure S7) except the high binding energy peak of 401.8 eV was assigned to NCR_4^+ (R = C, H). Detailed XPS peak fits of all regions are presented in Figures S5–S7 and Tables S1–S3. TiCN was observed in all samples at approximately 20 at. %. Interestingly, the N–O bond was observed in both samples, suggesting the possible formation of oxynitrides. When comparing atomic concentrations obtained from the XPS spectra, we observed that the C/N ratio is not unity and varies in a range close to 1.2–1.5:0.5 (see Tables S1–S3). We believe that the different C/N ratios can affect the optoelectronic properties of Ti_3CNT_x and other carbonitride MXenes in general, as will be discussed in the next section. The absence of Al confirms successful etching, washing, and delamination steps for both

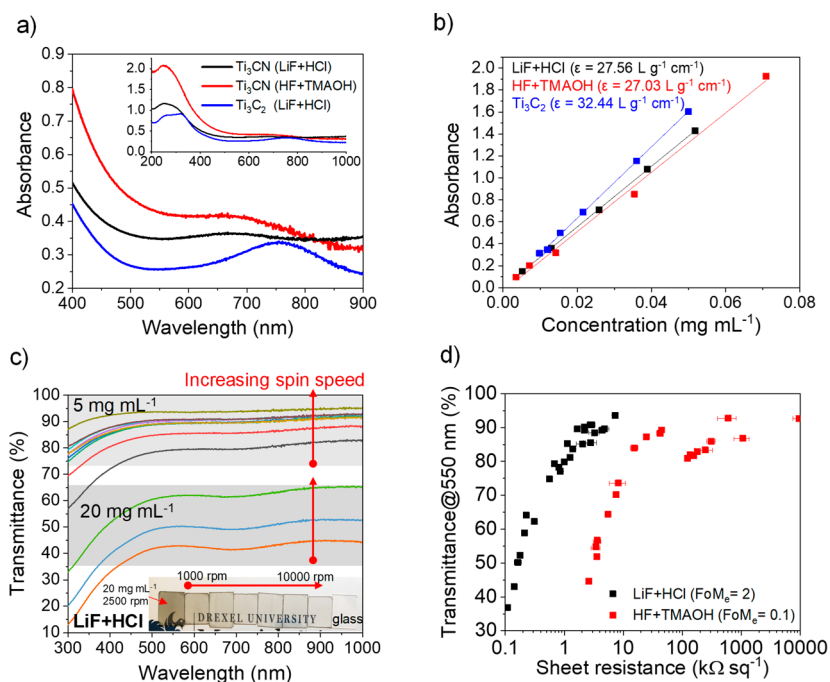


Figure 6. (a) UV–visible spectra of d-Ti₃CNT_x solutions produced using LiF + HCl (black) and HF + TMAOH (red) routes compared to Ti₃C₂T_x (LiF + HCl) solution (blue). The solution concentration is around 1.5×10^{-2} mg mL⁻¹. (b) Calibration curves of the solutions obtained using their respective peak absorption in the visible region. (c) UV–visible spectra of spin-casted Ti₃CNT_x (LiF + HCl) films. The optical image of the films is shown in the inset. Drexel University logo is used with permission from Drexel University. (d) Film transmittance as a function of sheet resistance for the Ti₃CNT_x samples prepared using two etching routes. Ti₃CNT_x (HF + TMAOH) thin films are about 10 times more resistive than Ti₃CNT_x (LiF + HCl) films.

synthesis methods, as they were adequate to remove any Al-containing impurities. From the Ti 2p region, it was observed that Ti in the HF + TMAOH and HF + TBAOH samples has higher contribution from Ti⁴⁺ (458.4 eV) of 17 and 26 at. %, respectively, compared to that of the LiF + HCl sample (13 at. %). The Ti⁴⁺ contribution could come from the O-terminated MXene surface and/or a small amount of TiO₂ nanoparticles present in the free-standing film samples used in XPS analysis. This might be due to treatment of the sample with bases, similar to that observed for the KOH- and NaOH-treated Ti₃C₂T_x.^{42,43}

Optoelectronic Properties. UV–visible spectroscopy was used to study the optical properties of Ti₃CNT_x prepared by different methods. Figure 6a shows absorption spectra of d-Ti₃CNT_x solutions prepared by LiF + HCl and HF + TMAOH methods compared to a solution of d-Ti₃C₂T_x prepared by the LiF + HCl method.³⁵ A clear distinction can be observed when comparing Ti₃CNT_x and Ti₃C₂T_x. The local absorption maxima are located at 670 and 770 nm for Ti₃CNT_x (LiF + HCl) and Ti₃C₂T_x (LiF + HCl), respectively. Ti₃CNT_x (HF + TMAOH) did not show a clear absorption peak, but a broader shoulder at around 670 nm. The difference in absorption peaks translates into different colors of the two MXenes, that is, brownish for Ti₃CNT_x and dark green for Ti₃C₂T_x as shown in Figure 4a. The full UV–visible spectra recorded over wavelengths between 200 and 1000 nm are shown in the inset of Figure 6a. It is worth mentioning that Ti₃CNT_x shows higher optical absorption in the near-infrared region compared to Ti₃C₂T_x, which could be useful for photothermal therapy applications. We also found that the absorption peak of Ti₃CNT_x made by LiF + HCl from different batches of Ti₃AlCN MAX powder showed a shift in peak position ranging from 670 to 730 nm (not shown). A conclusive reason for this

shift could not be drawn at this point and is beyond the scope of this study. However, we believe that it is related to the C/N ratio variation in the Ti₃AlCN MAX precursor. Further studies will be conducted to verify this hypothesis. In general, the results presented here show the tunability of optical properties of MXenes by manipulating their X elements. Figure 6b presents a plot of the absorbance at the local absorption maxima (670 nm for Ti₃CNT_x and 770 nm for Ti₃C₂T_x) as a function of the solution concentration and the extinction coefficients were calculated to be 27.6, 27.0, and 32.4 L g⁻¹ cm⁻¹ for Ti₃CNT_x (LiF + HCl), Ti₃CNT_x (HF + TMAOH), and Ti₃C₂T_x (LiF + HCl), respectively. Although the etching methods only slightly affected the absorption coefficient of Ti₃CNT_x, the resulting absorption coefficients were lower than that of Ti₃C₂T_x, which is beneficial for transparent conductive coating applications.

The transparent films of Ti₃CNT_x were prepared by a spin-casting technique using d-Ti₃CNT_x solution with a concentration between 5 and 20 mg mL⁻¹. As the TBAOH delamination route did not yield high-concentration solutions, we only compared the optoelectronic properties of thin films made by LiF + HCl and HF + TMAOH routes. When using 5 mg mL⁻¹ solution of Ti₃CNT_x (LiF + HCl), the transmittance of the thin films at 550 nm ranged from ~75 to 94%, when the spin speed increased from 1000 to 10 000 rpm. To obtain less transparent and more conductive films, 20 mg mL⁻¹ solution was used (Figure 6c). The thickness of the film with 80% transmittance was 9 nm with a surface roughness of 2.7 nm, while that of the film with 94% transmittance was 2.5 nm. The latter film mainly had a monolayer coverage of the MXene flakes as confirmed by AFM images (Figure S8). Although the thickest film we obtained with the 20 mg mL⁻¹ solution has a transparency of 40%, thicker films can be prepared by

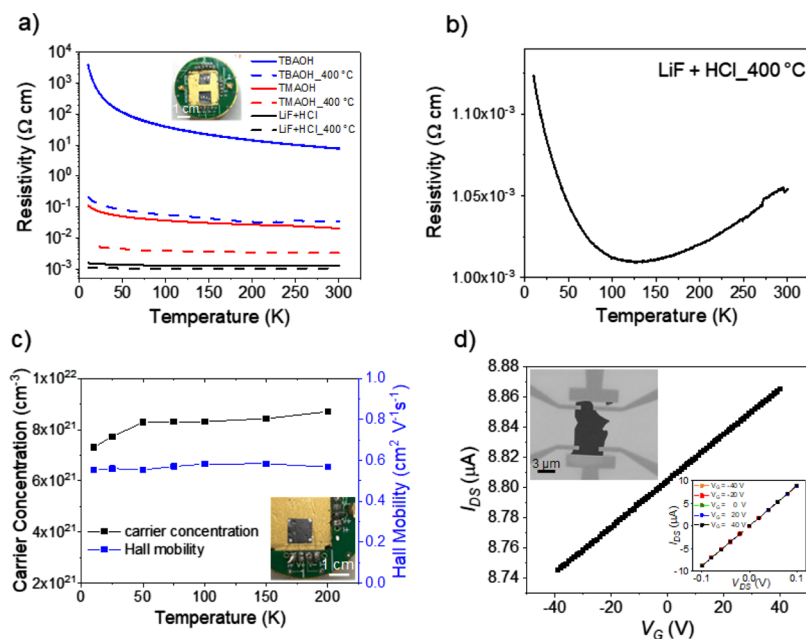


Figure 7. (a) Temperature-dependent resistivity of the Ti₃CNT_x films prepared by different routes. (b) Temperature-dependent resistivity of the Ti₃CNT_x (LiF + HCl) film after annealing at 400 °C in Ar, showing metallic behavior from room temperature to ~100 K. (c) Hall mobility and carrier concentration of the Ti₃CNT_x (LiF + HCl) film at different temperatures. (d) Transfer characteristics of a Ti₃CNT_x (LiF + HCl) single-flake device. Top inset is the SEM image of a four-terminal device and bottom inset is I_{DS} – V_{DS} curves for different gate voltages, which demonstrate Ohmic behavior and weak gate voltage dependence, indicating metallic behavior.

repeating the spin-casting process or using a higher solution concentration. Note that a high spin speed of more than 5000 rpm is required to obtain homogeneous coating when using high concentration of the MXene solution because of its viscoelastic property.⁴⁴ Moreover, we note that MXene in solution tends to agglomerate when the concentration of the solution exceeds 20 mg mL⁻¹, which may cause inhomogeneity of the resulting thin films.

Next, we studied the optoelectronic properties of the Ti₃CNT_x thin films by comparing their optical transparency measured by UV–visible spectroscopy and sheet resistance measured in a four-point probe configuration. The plots of transmittance as a function of sheet resistance of the thin films prepared from Ti₃CNT_x (LiF + HCl) and Ti₃CNT_x (HF + TMAOH) are shown in Figure 6d. At the same transparency, the films made from the Ti₃CNT_x (HF + TMAOH) solution were approximately 1 order of magnitude less conductive than those made from the LiF + HCl solution. The sheet resistance of the thin films with transparency between ~40 and ~94% prepared from the Ti₃CNT_x (LiF + HCl) solution ranges from 0.1 to 10 kΩ sq⁻¹, whereas that of films prepared from the Ti₃CNT_x (HF + TMAOH) solution range from 3 to 10 000 kΩ sq⁻¹. The electrical figure of merit (FoM_e; σ_{DC}/σ_{op} , where σ_{DC} is the electronic conductivity and σ_{op} is the optical conductivity at 550 nm) of each film was calculated using the equation $T_{550nm} = \left(1 + \frac{188.5 \sigma_{op}}{R_s \sigma_{DC}}\right)^{-2}$, where T_{550nm} is the transmittance of the film at 550 nm and R_s is the sheet resistance (Ω sq⁻¹).⁴⁵ The films prepared from the Ti₃CNT_x (LiF + HCl) solution and the Ti₃CNT_x (HF + TMAOH) solution have FoM_e values of 2 ± 0.81 and 0.1 ± 0.027 , respectively. The large difference in the electrical conductivities of the films prepared from the Ti₃CNT_x (LiF + HCl) and the Ti₃CNT_x (HF + TMAOH) solutions is ascribed to differences in their surface chemistries and largely to intercalation of

TMA⁺ cations, which expands the interlayer distance, suppressing inter-flake electron transport. However, we do not eliminate the possibility that the Ti₃CNT_x (HF + TMAOH) films could be more oxidized because of prolonged exposure to basic solution as suggested by the XPS results. Moreover, it was reported for Ti₃C₂T_x that HF etching results in more defective MXene flakes, which could potentially affect the electronic properties of MXenes.⁴⁶ The Ti₃CNT_x (LiF + HCl) thin films were less conductive than the Ti₃C₂T_x films of similar thickness that were prepared by a similar method.^{8,47} This is possibly due to reduced electron density of Ti d-electrons induced by the presence of highly electronegative nitrogen atoms in the X layer, as predicted by the DFT calculations.¹³ Although nitrogen has one extra electron compared to carbon, its electrons are localized in a lower energy band far away from the Fermi level, which are not active in electronic transport.¹³ Moreover, random distribution of the nitrogen atoms in the X layer and atomic defects could act as scattering centers, reducing electron mobility.^{13,25,48}

To study the stability of the Ti₃CNT_x thin films prepared by different methods, the resistance of the films with different thicknesses was recorded while the films were exposed to ambient conditions (20 °C, laboratory air). For Ti₃CNT_x (LiF + HCl) and Ti₃CNT_x (HF + TMAOH) films with 8 nm nominal thickness, the sheet resistance increased 1.25 and 1.5 times their original values after 30 h, respectively, as shown in Figure S9. For thinner films, the sheet resistance increased drastically over time, that is, 2.5 times for the Ti₃CNT_x (HF + TMAOH) film with ~4 nm thickness and 3.5 times for the Ti₃CNT_x (LiF + HCl) film with ~2 nm thickness. The Ti₃CNT_x thin films are less stable compared to Ti₃C₂T_x, where only 10% change was observed in a single-flake device over 30 h and a negligible change in resistance was observed in a 25 nm-thick film over 150 min.^{9,47} We also observed that vacuum annealing of the freshly made thin films of Ti₃CNT_x at 150 °C

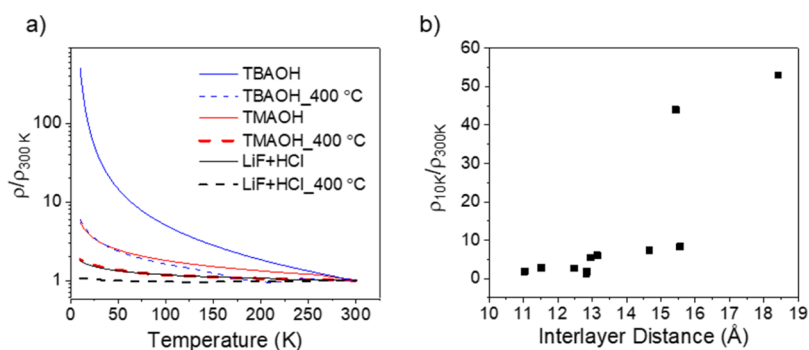


Figure 8. (a) Normalized low-temperature resistivity (ρ/ρ_{300K}) of the Ti_3CNT_x films prepared by different methods and post-synthesis treatments. (b) Correlation between ρ_{10K}/ρ_{300K} and interlayer distance obtained from XRD measurements. The resistivity ratio increased with increasing the interlayer distance, suggesting that the inter-flake electron hopping process limits the temperature-dependent macroscopic electronic conductivity.

Table 1. Summary of the Effects of Synthesis and Processing on Optoelectronic Properties of Ti_3CNT_x

etching	delamination	annealing conditions	optical absorption peak (nm)	interlayer distance (Å)	room-temperature resistivity (Ω cm)	ρ_{10K}/ρ_{300K}
LiF + HCl		as-produced	670	13.0	1.1×10^{-3}	1.80
		400 °C	N/A	10.3	1.0×10^{-3}	1.07
HF	TMAOH	as-produced	670	13.0, 16.1	2.0×10^{-2}	5.50
		400 °C	N/A	11.0	3.3×10^{-3}	1.84
HF	TBAOH	as-produced	N/A	18.7	7.8	480
		400 °C	N/A	13.0	3.4×10^{-2}	6.06

caused the sheet resistance to increase, opposite to that reported for $Ti_3C_2T_x$.⁸ The increase of sheet resistance was only observed for the very thin films (<20 nm). As we discuss in the next section, annealing of the micrometer-thick filtered films reduced their sheet resistance.

Electronic and Transport Properties. Electronic and transport properties of free-standing MXene films were studied to provide insights into the role of the X site composition on electronic behavior. The MXene films made by vacuum-assisted filtration of d- Ti_3CNT_x solution with a thickness between 5 and 10 μ m were wired to a PPMS puck in a four-point configuration using a silver wire and a silver paint, as shown in the inset of Figure 7a. Temperature-dependent resistivity (ρ versus T) was measured from 10 to 300 K with a cooling/heating rate of 5 K min^{-1} (Figure 7a). For each synthesis route, we tested the as-produced films (solid lines) and the same films after annealing at 400 °C for 3 h in Ar environment (dashed lines). The room-temperature resistivity of Ti_3CNT_x (HF + TBAOH) with the value of 7.8 Ω cm was the highest among the as-produced films, followed by the Ti_3CNT_x (HF + TMAOH) at 2.0×10^{-2} Ω cm, and the Ti_3CNT_x (LiF + HCl) sample at 1.1×10^{-3} Ω cm. After annealing at 400 °C, about 3 orders of magnitude decrease in resistivity was observed for the Ti_3CNT_x (HF + TBAOH) film and 1 order of magnitude decrease for the Ti_3CNT_x (HF + TMAOH) film, whereas that of the Ti_3CNT_x (LiF + HCl) film remained almost unchanged. The decrease in resistivity corresponds to the decomposition/desorption of the intercalated molecules as revealed by the XRD (Figure 5a) and the TGA-MS (Figures 5b,d and S3a) results discussed earlier. Interestingly, all the as-produced films displayed a negative slope of ρ versus T ($d\rho/dT$) over the temperature range measured.

For comparison, using the ρ versus T data shown in Figure 7a, the low-temperature resistivity was normalized by the

room-temperature resistivity (ρ/ρ_{300K}) and presented in Figure 8a. The ratios of resistivity at 10 K to room-temperature resistivity are 480, 5.5, and 1.8 for the Ti_3CNT_x (HF + TBAOH), Ti_3CNT_x (HF + TMAOH), and Ti_3CNT_x (LiF + HCl) films before annealing, respectively. The (ρ/ρ_{300K}) versus T data of the Ti_3CNT_x (HF + TBAOH) film after annealing can be almost superimposed with that of the Ti_3CNT_x (HF + TMAOH) film before annealing. These two films also exhibited similar interlayer distances as shown in Figure 5a. A similar behavior was also observed when comparing the Ti_3CNT_x (HF + TMAOH) film after annealing with the as-produced Ti_3CNT_x (LiF + HCl) film. These results suggest that temperature-dependent resistivity is largely governed by the inter-flake transport process, which is strongly affected by the interlayer distance. A similar increase of resistivity with increasing interlayer distance was also observed for $Ti_3C_2T_x$ treated with long-chain alkylammonium salts.¹⁵ We also observed a correlation between the interlayer distance and the ratio of the resistivity at 10 K to the room-temperature resistivity (ρ_{10K}/ρ_{300K}) as shown in Figure 8b, where an abrupt increase of ρ_{10K}/ρ_{300K} occurred when the interlayer distance exceeded 15 Å. Strikingly, the initially negative $d\rho/dT$ of the as-produced Ti_3CNT_x (LiF + HCl) film changed to positive $d\rho/dT$ after annealing at 400 °C. As shown in Figure 7b, the resistivity decreased with decreasing temperature from 300 to 100 K but increased as the temperature further decreased to 10 K. A similar rise in the resistivity at low temperature was also observed for the $Ti_3C_2T_x$ MXene, which was attributed to weak localization.^{14,49} We note in passing that the increase of resistivity with decreasing temperature of the as-produced Ti_3CNT_x MXene does not originate from the existence of a band gap of the material but most probably because of the inter-flake electron hopping. For a better comparison, the effects of synthesis and processing on the optical and electronic properties of Ti_3CNT_x are summarized in Table 1.

To study the effects of ion exchange on the electronic properties, the Ti_3CNT_x (HF + TBAOH) film was treated with 1 M HCl for 3 h to remove intercalated TBA^+ ions and subsequently dried at 150 °C. The XRD results shown in Figure S10a reveal a shift from 4.8° of the as-produced film (also dried at 150 °C) to a broad peak centered around 5.7° after the HCl treatment. The corresponding ρ versus T of the TBAOH-delaminated films with acid and heat treatments are shown in Figure S10b. The data for the as-produced HF + TBAOH film annealed at 400 °C are shown for comparison. A similar correlation between the interlayer distance and resistivity, that is, the larger the interlayer distance, the higher the room-temperature resistivity and the larger the negative slope of the ρ versus T , was observed for the Ti_3CNT_x (LiF + HCl) film treated with TBAOH for 24 h (Figure S10c,d). Note that the HCl treatment of the Ti_3CNT_x (LiF + HCl) film neither altered the interlayer distance nor the resistivity of the film, suggesting that the intercalated Li^+ ions did not undergo ion exchange with protons of HCl.

To study the carrier densities and mobilities of Ti_3CNT_x , we performed Hall measurements on the as-produced Ti_3CNT_x (LiF + HCl) film at various temperatures (Figure 7c). The Hall mobility was almost constant at $0.6 \text{ cm}^2 \text{ V}^{-1} \text{ s}^{-1}$ from 10 to 200 K, whereas the carrier concentration increased slightly from $7.7 \times 10^{21} \text{ cm}^{-3}$ at 10 K to $8.7 \times 10^{21} \text{ cm}^{-3}$ at 200 K. The data above 200 K were too noisy to make any meaningful interpretation. The high carrier concentration is consistent with a metallic band structure of the Ti_3CNT_x film, even though this sample showed negative $d\rho/dT$ macroscopic resistivity behavior in the ρ versus T measurement. Moreover, the negative Hall slope (Figure S11b,d) indicates that electrons are the majority carrier, similar to that observed for $\text{Ti}_3\text{C}_2\text{T}_x$.⁴⁷ The combination of the Hall and resistivity results strongly suggests that Ti_3CNT_x is intrinsically metallic with a large electron density as predicted by DFT.^{13,48} However, expansion of the interlayer distance caused by the intercalation of water and organic molecules leads to the macroscopic negative $d\rho/dT$ that might be misinterpreted as semiconductor behavior.

To study the intrinsic electronic and transport properties of Ti_3CNT_x , we measured the conductivity of five two-terminal (2T) and two four-terminal (4T) field-effect transistors, which were fabricated using single flakes of Ti_3CNT_x (LiF + HCl); see the inset in Figure 7d for an SEM image of a typical 4T device. The results of electrical measurements for all devices at room temperature are summarized in Table S4. In all studied devices, the drain–source current (I_{DS}) linearly depends on the drain–source voltage (V_{DS}), which indicates Ohmic behavior. The calculated average sheet resistance is $8900 \text{ } \Omega \text{ sq}^{-1}$, which is 3–4 times higher than that of $\text{Ti}_3\text{C}_2\text{T}_x$ single flakes.⁹ Using a flake thickness of 1 nm, the single-flake resistivity was calculated to be $8.9 \times 10^{-4} \text{ } \Omega \text{ cm}$. We also investigated the transfer characteristics of the Ti_3CNT_x devices by measuring I_{DS} while applying gate voltage (V_{G}) to the bottom electrode. As can be seen in Figure 7d, I_{DS} increases with increasing V_{G} and the positive slope indicates that electrons are the majority charge carriers, in agreement with the Hall measurements on a free-standing film. The field-effect mobility was calculated to be $1.4 \pm 0.25 \text{ cm}^2 \text{ V}^{-1} \text{ s}^{-1}$ (Table S4), which is reasonable given that the inter-flake resistance reduces carrier mobility measured in a Hall measurement of a free-standing film. This value is comparable to the values of 2.6 ± 0.7 and $0.7 \pm 0.2 \text{ cm}^2 \text{ V}^{-1} \text{ s}^{-1}$ obtained in similar measurements for devices based on single flakes of $\text{Ti}_3\text{C}_2\text{T}_x$.^{9,50}

CONCLUSIONS

A systematic study of the effect of synthesis (LiF + HCl or HF) and processing (intercalation, annealing, drying, and ion exchange) on optoelectronic properties of the Ti_3CNT_x MXene has been conducted, which showed that Ti_3CNT_x exhibited lower electronic conductivity and a blue shift in UV–visible spectra compared to its $\text{Ti}_3\text{C}_2\text{T}_x$ carbide counterpart. This work has demonstrated that the optoelectronic properties of MXenes can be controlled by manipulating the X element (C versus N). We also showed that increasing the interlayer distance by intercalants, such as water, TMAOH, and TBAOH, decreases the electronic conductivity because of increased inter-flake resistance. The inter-flake process strongly affects the temperature-dependent resistivity, causing the macroscopic negative slope ($d\rho/dT$) observed in the as-produced Ti_3CNT_x samples. Removal of intercalants by vacuum annealing or ion exchange resulted in several orders of magnitude increase in conductivity of the organic-intercalated samples and caused the macroscopic conductivity within the Ti_3CNT_x (LiF + HCl) sample to change to metallic behavior. The Hall measurements indicated electrons as the majority charge carrier with a density close to $8 \times 10^{21} \text{ cm}^{-3}$, which is in good agreement with the electronic transport measurements of field-effect transistors made from single MXene flakes, showing that Ti_3CNT_x is intrinsically metallic within the flake.

ASSOCIATED CONTENT

Supporting Information

The Supporting Information is available free of charge on the ACS Publications website at DOI: 10.1021/acs.chemmater.9b00401.

Additional material characterizations including XRD, SEM, AFM, TGA–MS, XPS, and electrical characterization of Ti_3CNT_x single-flake devices; XRD pattern and resistivity of Ti_3AlCN MAX phase; AFM images of Ti_3CNT_x single-flake devices; TGA–MS thermograms of Ti_3CNT_x (HF + TBAOH) and TBAOH solution; XRD pattern and SEM image of Ti_3CNT_x and $\text{Ti}_3\text{C}_2\text{T}_x$ after annealing at 1500 °C; XPS spectra of Ti_3CNT_x synthesized by LiF + HCl, HF + TMAOH, and HF + TBAO; peak assignments of XPS spectra; AFM images of Ti_3CNT_x thin films; change in resistance with time of the Ti_3CNT_x thin films; XRD patterns and temperature-dependent resistivity of Ti_3CNT_x after chemical treatments; examples of Hall effect data of the Ti_3CNT_x (LiF + HCl) film; and results of electrical measurements for all single-flake Ti_3CNT_x FET devices (PDF)

AUTHOR INFORMATION

Corresponding Author

*E-mail: gogotsi@drexel.edu.

ORCID

Kanit Hantanasirisakul: 0000-0002-4890-1444

Mohamed Alhabeab: 0000-0002-9460-8548

Alexey Lipatov: 0000-0001-5043-1616

Kathleen Maleski: 0000-0003-4032-7385

Babak Anasori: 0000-0002-1955-253X

Alexander Sinitiskii: 0000-0002-8688-3451

Yury Gogotsi: 0000-0001-9423-4032

Notes

The authors declare no competing financial interest.

ACKNOWLEDGMENTS

This work is supported by the U.S. Department of Energy (DOE), Office of Science, Office of Basic Energy Sciences, grant no. DE-SC0018618. A.L. and A.S. acknowledge the support from Nebraska Public Power District through the Nebraska Center for Energy Sciences Research (NCESR) and the National Science Foundation through the Nebraska Materials Research Science and Engineering Center (MRSEC; DMR-1420645). The TEM imaging, device fabrication, and characterization were performed using instrumentation at the Nebraska Nanoscale Facility, which is supported by the NSF (ECCS-1542182) and the Nebraska Research Initiative. C.I. and P.P. acknowledge the support from the Science Achievement Scholarship of Thailand and the Center of Excellence for Innovation in Chemistry, Faculty of Science, Mahidol University. Prof. Goran Karapetrov (Drexel University) is acknowledged for providing access to AFM machine, and Asia Sarycheva is acknowledged for help with AFM measurements. Dr. Mykola Seredych is acknowledged for proof-reading the manuscript. Drexel University Core Facilities are acknowledged for providing access to XPS, SEM, and XRD instruments.

REFERENCES

- (1) Anasori, B.; Lukatskaya, M. R.; Gogotsi, Y. 2D Metal Carbides and Nitrides (MXenes) for Energy Storage. *Nat. Rev. Mater.* **2017**, *2*, 16098.
- (2) Shahzad, F.; Alhabeab, M.; Hatter, C. B.; Anasori, B.; Man Hong, S.; Koo, C. M.; Gogotsi, Y. Electromagnetic Interference Shielding with 2D Transition Metal Carbides (MXenes). *Science* **2016**, *353*, 1137–1140.
- (3) Huang, K.; Li, Z.; Lin, J.; Han, G.; Huang, P. Two-dimensional Transition Metal Carbides and Nitrides (MXenes) for Biomedical Applications. *Chem. Soc. Rev.* **2018**, *47*, 5109–5124.
- (4) Hantanasirisakul, K.; Zhao, M.-Q.; Urbankowski, P.; Halim, J.; Anasori, B.; Kota, S.; Ren, C. E.; Barsoum, M. W.; Gogotsi, Y. Fabrication of $Ti_3C_2T_x$ MXene Transparent Thin Films with Tunable Optoelectronic Properties. *Adv. Electron. Mater.* **2016**, *2*, 1600050.
- (5) Srimuk, P.; Kaasik, F.; Krüner, B.; Tolosa, A.; Fleischmann, S.; Jäckel, N.; Tekeli, M. C.; Aslan, M.; Suss, M. E.; Presser, V. MXene as a Novel Intercalation-type Pseudocapacitive Cathode and Anode for Capacitive Deionization. *J. Mater. Chem. A* **2016**, *4*, 18265–18271.
- (6) Wang, H.; Wu, Y.; Yuan, X.; Zeng, G.; Zhou, J.; Wang, X.; Chew, J. W. Clay-Inspired MXene-Based Electrochemical Devices and Photo-Electrocatalyst: State-of-the-Art Progresses and Challenges. *Adv. Mater.* **2018**, *30*, e1704561.
- (7) Hantanasirisakul, K.; Gogotsi, Y. Electronic and Optical Properties of Two-Dimensional Transition Metal Carbides and Nitrides (MXenes). *Adv. Mater.* **2018**, *30*, 1804779.
- (8) Zhang, C. J.; Anasori, B.; Seral-Ascaso, A.; Park, S.-H.; McEvoy, N.; Shmeliov, A.; Duesberg, G. S.; Coleman, J. N.; Gogotsi, Y.; Nicolosi, V. Transparent, Flexible, and Conductive 2D Titanium Carbide (MXene) Films with High Volumetric Capacitance. *Adv. Mater.* **2017**, *29*, 1702678.
- (9) Lipatov, A.; Alhabeab, M.; Lukatskaya, M. R.; Boson, A.; Gogotsi, Y.; Sinitskii, A. Effect of Synthesis on Quality, Electronic Properties and Environmental Stability of Individual Monolayer Ti_3C_2 MXene Flakes. *Adv. Electron. Mater.* **2016**, *2*, 1600255.
- (10) Maleski, K.; Ren, C. E.; Zhao, M.-Q.; Anasori, B.; Gogotsi, Y. Size-Dependent Physical and Electrochemical Properties of Two-Dimensional MXene Flakes. *ACS Appl. Mater. Interfaces* **2018**, *10*, 24491–24498.
- (11) Hart, J. L.; Hantanasirisakul, K.; Lang, A. C.; Anasori, B.; Pinto, D.; Pivak, Y.; van Omme, J. T.; May, S. J.; Gogotsi, Y.; Taheri, M. L. Control of MXenes' Electronic Properties Through Termination and Intercalation. *Nat. Commun.* **2019**, *10*, 522.
- (12) Khazaei, M.; Ranjbar, A.; Arai, M.; Sasaki, T.; Yunoki, S. Electronic Properties and Applications of MXenes: a Theoretical Review. *J. Mater. Chem. C* **2017**, *5*, 2488–2503.
- (13) Enyashin, A. N.; Ivanovskii, A. L. Two-dimensional Titanium Carbonitrides and Their Hydroxylated Derivatives: Structural, Electronic Properties and Stability of MXenes $Ti_3C_2-xN_x(OH)_2$ from DFTB Calculations. *J. Solid State Chem.* **2013**, *207*, 42–48.
- (14) Anasori, B.; Shi, C.; Moon, E. J.; Xie, Y.; Voigt, C. A.; Kent, P. R. C.; May, S. J.; Billinge, S. J. L.; Barsoum, M. W.; Gogotsi, Y. Control of Electronic Properties of 2D Carbides (MXenes) by Manipulating Their Transition Metal Layers. *Nanoscale Horiz.* **2016**, *1*, 227–234.
- (15) Ghidui, M.; Kota, S.; Halim, J.; Sherwood, A. W.; Nedfors, N.; Rosen, J.; Mochalin, V. N.; Barsoum, M. W. Alkylammonium Cation Intercalation into Ti_3C_2 (MXene): Effects on Properties and Ion-Exchange Capacity Estimation. *Chem. Mater.* **2017**, *29*, 1099–1106.
- (16) Römer, F. M.; Wiedwald, U.; Strusch, T.; Halim, J.; Mayerberger, E.; Barsoum, M. W.; Farle, M. Controlling the Conductivity of Ti_3C_2 MXenes by Inductively Coupled Oxygen and Hydrogen Plasma Treatment and Humidity. *RSC Adv.* **2017**, *7*, 13097–13103.
- (17) Lengauer, W. *Transition Metal Carbides, Nitrides, and Carbonitrides*; Wiley-VCH Weinheim: Germany, 2008.
- (18) Barbier, E.; Thevenot, F. Electrical Resistivity in the Titanium Carbonitride-zirconia System. *J. Mater. Sci.* **1992**, *27*, 2383–2388.
- (19) Guemaz, M.; Moraitis, G.; Mosser, A.; Khan, M. A.; Parlebas, J. C. Band Structure of Substoichiometric Titanium Nitrides and Carbonitrides: Spectroscopic and Theoretical Investigations. *J. Phys.: Condens. Matter* **1997**, *9*, 8453.
- (20) *Materials Science of Carbides, Nitrides and Borides*; Gogotsi, Y., Andrievski, R. A., Eds.; Kluwer: Dordrecht, Netherlands, 1999.
- (21) Barsoum, M. W. The $M_{N+1}AX_N$ Phases: A New Class of Solids. *Prog. Solid State Chem.* **2000**, *28*, 201–281.
- (22) Finkel, P.; Barsoum, M. W.; Hettinger, J. D.; Lofland, S. E.; Yoo, H. I. Low-temperature Transport Properties of Nanolaminates Ti_3AlC_2 and Ti_4AlN_3 . *Phys. Rev. B: Condens. Matter Mater. Phys.* **2003**, *67*, 235108.
- (23) Hettinger, J. D.; Lofland, S. E.; Finkel, P.; Meehan, T.; Palma, J.; Harrell, K.; Gupta, S.; Ganguly, A.; El-Raghy, T.; Barsoum, M. W. Electrical Transport, Thermal Transport, and Elastic Properties of M_2AlC ($M=Ti, Cr, Nb$, and V). *Phys. Rev. B: Condens. Matter Mater. Phys.* **2005**, *72*, 115120.
- (24) Finkel, P.; Seaman, B.; Harrell, K.; Palma, J.; Hettinger, J. D.; Lofland, S. E.; Ganguly, A.; Barsoum, M. W.; Sun, Z.; Li, S.; Ahuja, R. Electronic, Thermal, and Elastic Properties of $Ti_3Si_{1-x}Ge_xC_2$ Solid Solutions. *Phys. Rev. B: Condens. Matter Mater. Phys.* **2004**, *70*, 085104.
- (25) Scarabozzi, T.; Ganguly, A.; Hettinger, J. D.; Lofland, S. E.; Amini, S.; Finkel, P.; El-Raghy, T.; Barsoum, M. W. Electronic and Thermal Properties of $Ti_3Al(C_{0.5}N_{0.5})_2$, $Ti_2Al(C_{0.5}N_{0.5})$ and Ti_2AlN . *J. Appl. Phys.* **2008**, *104*, 073713.
- (26) Du, F.; Tang, H.; Pan, L.; Zhang, T.; Lu, H.; Xiong, J.; Yang, J.; Zhang, C. Environmental Friendly Scalable Production of Colloidal 2D Titanium Carbonitride MXene with Minimized Nanosheets Restacking for Excellent Cycle Life Lithium-Ion Batteries. *Electrochim. Acta* **2017**, *235*, 690–699.
- (27) Huang, B.; Zhou, N.; Chen, X.; Ong, W. J.; Li, N. Insights into the Electrocatalytic Hydrogen Evolution Reaction Mechanism on Two-Dimensional Transition-Metal Carbonitrides (MXene). *Chem.—Eur. J.* **2018**, *24*, 18479–18486.
- (28) Zhang, W.; Cheng, C.; Fang, P.; Tang, B.; Zhang, J.; Huang, G.; Cong, X.; Zhang, B.; Ji, X.; Miao, L. The Role of Terminations and Coordination Atoms on the Pseudocapacitance of Titanium Carbonitride Monolayers. *Phys. Chem. Chem. Phys.* **2016**, *18*, 4376–4384.
- (29) Urbankowski, P.; Anasori, B.; Hantanasirisakul, K.; Yang, L.; Zhang, L.; Haines, B.; May, S. J.; Billinge, S. J. L.; Gogotsi, Y. 2D Molybdenum and Vanadium Nitrides Synthesized by Ammoniation of

2D Transition Metal Carbides (MXenes). *Nanoscale* **2017**, *9*, 17722–17730.

(30) Mashtalir, O.; Naguib, M.; Mochalin, V. N.; Dall'Agnese, Y.; Heon, M.; Barsoum, M. W.; Gogotsi, Y. Intercalation and Delamination of Layered Carbides and Carbonitrides. *Nat. Commun.* **2013**, *4*, 1716.

(31) Naguib, M.; Unocic, R. R.; Armstrong, B. L.; Nanda, J. Large-scale Delamination of Multi-layers Transition Metal Carbides and Carbonitrides "MXenes". *Dalton Trans.* **2015**, *44*, 9353–9358.

(32) Naguib, M.; Mashtalir, O.; Carle, J.; Presser, V.; Lu, J.; Hultman, L.; Gogotsi, Y.; Barsoum, M. W. Two-dimensional Transition Metal Carbides. *ACS Nano* **2012**, *6*, 1322–1331.

(33) Miccoli, I.; Edler, F.; Pfnür, H.; Tegenkamp, C. The 100th Anniversary of the Four-point Probe Technique: the Role of Probe Geometries in Isotropic and Anisotropic systems. *J. Phys.: Condens. Matter* **2015**, *27*, 223201.

(34) Barsoum, M. W. *MAX Phases: Properties of Machinable Ternary Carbides and Nitrides*; Wiley-VCH: Weinheim, Germany, 2013.

(35) Alhabet, M.; Maleski, K.; Anasori, B.; Lelyukh, P.; Clark, L.; Sin, S.; Gogotsi, Y. Guidelines for Synthesis and Processing of 2D Titanium Carbide ($\text{Ti}_3\text{C}_2\text{T}_x$ MXene). *Chem. Mater.* **2017**, *29*, 7633–7644.

(36) Lipatov, A.; Lu, H.; Alhabet, M.; Anasori, B.; Gruverman, A.; Gogotsi, Y.; Sinitiskii, A. Elastic Properties of 2D $\text{Ti}_3\text{C}_2\text{T}_x$ MXene Monolayers and Bilayers. *Sci. Adv.* **2018**, *4*, eaat0491.

(37) Wang, X.; Shen, X.; Gao, Y.; Wang, Z.; Yu, R.; Chen, L. Atomic-scale Recognition of Surface Structure and Intercalation Mechanism of $\text{Ti}_3\text{C}_2\text{X}$. *J. Am. Chem. Soc.* **2015**, *137*, 2715–2721.

(38) Ochedowski, O.; Bussmann, B. K.; Schleberger, M. Graphene on Mica—Intercalated Water Trapped for Life. *Sci. Rep.* **2015**, *4*, 6003.

(39) Novoselov, K. S.; Jiang, D.; Schedin, F.; Booth, T. J.; Khotkevich, V. V.; Morozov, S. V.; Geim, A. K. Two-dimensional Atomic Crystals. *Proc. Natl. Acad. Sci. U.S.A.* **2005**, *102*, 10451–10453.

(40) Ghidui, M.; Halim, J.; Kota, S.; Bish, D.; Gogotsi, Y.; Barsoum, M. W. Ion-Exchange and Cation Solvation Reactions in Ti_3C_2 MXene. *Chem. Mater.* **2016**, *28*, 3507–3514.

(41) McCleskey, E. W.; Almers, W. The Ca Channel in Skeletal Muscle is a Large Pore. *Proc. Natl. Acad. Sci. U.S.A.* **1985**, *82*, 7149–7153.

(42) Dall'Agnese, Y.; Lukatskaya, M. R.; Cook, K. M.; Taberna, P.-L.; Gogotsi, Y.; Simon, P. High Capacitance of Surface-modified 2D Titanium Carbide in Acidic Electrolyte. *Electrochem. Commun.* **2014**, *48*, 118–122.

(43) Li, T.; Yao, L.; Liu, Q.; Gu, J.; Luo, R.; Li, J.; Yan, X.; Wang, W.; Liu, P.; Chen, B.; Zhang, W.; Abbas, W.; Naz, R.; Zhang, D. Fluorine-Free Synthesis of High-Purity $\text{Ti}_3\text{C}_2\text{T}_x$ (T=OH, O) via Alkali Treatment. *Angew. Chem., Int. Ed.* **2018**, *57*, 6115–6119.

(44) Akuzum, B.; Maleski, K.; Anasori, B.; Lelyukh, P.; Alvarez, N. J.; Kumbur, E. C.; Gogotsi, Y. Rheological Characteristics of 2D Titanium Carbide (MXene) Dispersions: A Guide for Processing MXenes. *ACS Nano* **2018**, *12*, 2685–2694.

(45) De, S.; Coleman, J. N. Are There Fundamental Limitations on the Sheet Resistance and Transmittance of Thin Graphene Films? *ACS Nano* **2010**, *4*, 2713–2720.

(46) Sang, X.; Xie, Y.; Lin, M.-W.; Alhabet, M.; Van Aken, K. L.; Gogotsi, Y.; Kent, P. R. C.; Xiao, K.; Unocic, R. R. Atomic Defects in Monolayer Titanium Carbide ($\text{Ti}_3\text{C}_2\text{T}_x$) MXene. *ACS Nano* **2016**, *10*, 9193–9200.

(47) Dillon, A. D.; Ghidui, M. J.; Krick, A. L.; Griggs, J.; May, S. J.; Gogotsi, Y.; Barsoum, M. W.; Fafarman, A. T. Highly Conductive Optical Quality Solution-Processed Films of 2D Titanium Carbide. *Adv. Funct. Mater.* **2016**, *26*, 4162–4168.

(48) Jhon, Y. I.; Koo, J.; Anasori, B.; Seo, M.; Lee, J. H.; Gogotsi, Y.; Jhon, Y. M. Metallic MXene Saturable Absorber for Femtosecond Mode-Locked Lasers. *Adv. Mater.* **2017**, *29*, 1702496.

(49) Halim, J.; Lukatskaya, M. R.; Cook, K. M.; Lu, J.; Smith, C. R.; Näslund, L.-Å.; May, S. J.; Hultman, L.; Gogotsi, Y.; Eklund, P.;

Barsoum, M. W. Transparent Conductive Two-Dimensional Titanium Carbide Epitaxial Thin Films. *Chem. Mater.* **2014**, *26*, 2374–2381.

(50) Miranda, A.; Halim, J.; Barsoum, M. W.; Lorke, A. Electronic Properties of Freestanding $\text{Ti}_3\text{C}_2\text{T}_x$ MXene Monolayers. *Appl. Phys. Lett.* **2016**, *108*, 033102.